ADVANCED MATERIALS INTERFACES
Open Access
www.advmatinterfaces.de

Anisotropic Tunability of Vibrational Modes in Black Phosphorus Under Uniaxial Compressive/Tensile Strain

Hao Li, Tayfun Kutlu, Félix Carrascoso, Hasan Sahin, Carmen Munuera, and Andrés Castellanos Gómez**

Strain engineering is a powerful strategy for tuning the optical, electrical, vibrational properties of 2D nanomaterials. In this work, a four-point bending apparatus is constructed to apply both compressive and tensile strain on 2D anisotropic black phosphorus flake. Further polarized Raman spectroscopy is used to study the vibrational modes of black phosphorus flakes under uniaxial strain applied along various crystalline orientations. Here, a strong anisotropic blue/redshift of A^1_g, B_{2g}, and A^2_g modes is found under compressive/tensile strain, respectively. Interestingly, mode A^1_g exhibits the maximum/minimum shift while mode B_{2g} and mode A^2_g present the minimum/maximum shift when the strain is applied along armchair/zigzag direction. Density functional theory calculations are carried out to investigate the anisotropic strain response mechanism, finding that the strain-induced regulation of the P—P bond angle, bond length, and especially interlayer interaction has a giant influence on the Raman shift.

1. Introduction

Strain engineering has proven to be an efficient strategy to tune the band structure and therefore the electrical, optical, physical, and vibrational properties of 2D materials,[1–4] thus opening the door to strain-tunable electronic and optoelectronic devices.[5–11] Note that 2D materials could sustain remarkable strains, up to 10–20% in principle,[12,13] offering a wide range of bandgap tunability. Additionally, 2D materials could be strained in various ways, such as homogenous/inhomogenous strain,[14–19] uniaxial/biaxial strain,[20–22], etc. Based on above, various strain systems were developed in order to meet the needs of users,[16,21,22] among them applying uniaxial strain through the bending of a flexible polymer substrate assisted by a multi-point bending setup has become a popular and efficient way to perform strain engineering experiments in 2D materials.

Most of the reported 2D materials-based strain engineering works are focused on 2D isotropic materials (graphene, TMDs, etc.).[23–28] For 2D materials with a strong in-plane anisotropy, theoretical studies have verified that the uniaxial strain is supposed to tune their properties differently along different crystalline directions providing an extra degree of freedom for the strain-induced tunability.[29,30] However, in the case of the experimental study, applying strain along different crystalline orientations of 2D anisotropic materials is still a challenge for common multi-points bending setups, which has restricted the strain engineering's development on anisotropic materials. Recent studies based on anisotropic materials are scarce and focus on the investigation of the effect of only uniaxial tensile strain.[31–34] In our latest works, we have developed a homebuilt three-point bending setup to study the effect of uniaxial tensile strain on the exciton shift of $ZrSe_3$ and ReS_2.[35,36] In those previous works, due to the geometry of the three-point bending setup, we could not apply compressive uniaxial strain that is still a barrier on having a comprehensive understanding of the effect of uniaxial strain on 2D anisotropic materials.

Herein, we have modified our angle-dependent bending setup to adopt a four-point bending setup geometry that is now compatible with both tensile and compressive uniaxial strains applied along different crystal directions. The four-point bending apparatus offers a new strategy to apply both compressive and tensile strain on the 2D anisotropic black phosphorus (BP), which shows a giant in-plane anisotropy with two specific crystalline directions: armchair (AC) and zigzag (ZZ) directions. In this work, we use polarized Raman spectroscopy to study the effect of the strain on the vibrational property of black phosphorus. The Raman peaks corresponding to mode A^1_g, mode B_{2g}, and mode A^2_g showed a clear anisotropic blueshift/redshift under

H. Li, F. Carrascoso, C. Munuera, A. Castellanos Gómez
Materials Science Factory
Instituto de Ciencia de Materiales de Madrid (ICMM-CSIC)
Madrid 28049, Spain
E-mail: hao.li@estudiante.uam.es; andres.castellanos@csic.es
T. Kutlu
Department of Physics
Izmir Institute of Technology
Izmir 35430, Turkey
H. Sahin
Department of Photonics
Izmir Institute of Technology
Izmir 35430, Turkey

The ORCID identification number(s) for the author(s) of this article can be found under https://doi.org/10.1002/admi.202300540

DOI: 10.1002/admi.202300540

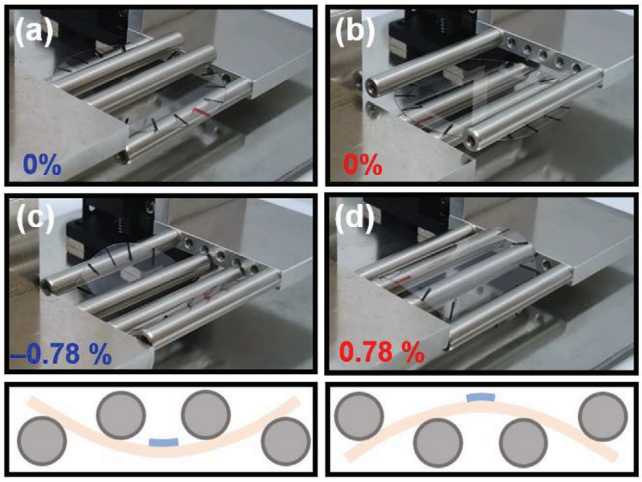

Figure 1. Setup details for angle-resolved uniaxial straining measurements. a,b) Pictures of a disk-like sample mounted between the pivotal points under strain of 0%, compression for (a), and tension for (b), respectively. Pictures of the sample upon c) −0.78% of compressive strain and d) 0.78% of tensile strain. The position of the red marker line on the edge of the disc-shaped substrate is used as a reference to determine the rotation angle of the substrate along the experiments, (a) and (b) show an example where the strain is applied along two orthogonal directions. The cartoons illustrate the strained states under compression and tension, respectively.

compressive/tensile strain along different directions. Interestingly, we found that when the strain was applied along the armchair direction of black phosphorus, mode A^1_g exhibited a maximum shift while mode B_{2g} and mode A^2_g presented a minimum shift. On the other hand, when strain was applied along the zigzag direction, the mode A^1_g showed a minimum shift while the shift of mode B_{2g} and mode A^2_g reached a maximum, which was investigated resulting from the strain's effect on the bond length and bond angle between phosphorus atoms. Therefore, uniaxial strain engineering could be studied in a comprehensive way with our four-point bending apparatus, which also paves a way to have a better understanding of other 2D anisotropic materials under strain.

2. Results and Discussion

Herein, once the target black phosphorus flake is found under optical microscope inspection, one can transfer the flake onto the center of a disk-like polycarbonate (PC) substrate (diameter of 5 cm), which is marked every 20° on the edge, by an all-dry deterministic placement method.[37] Further, the sample is mounted onto a homebuilt four-point bending setup as Figure S1 (Supporting Information) shows. By adjusting the relative height between the inner and outer cylinders one can apply compressive strain (**Figure 1**c) and tensile strain (Figure 1d). For this homebuilt four-points bending setup, the uniaxial strain ϵ could be applied by displacing two outer cylinders with two inner cylinders fixed and calculated as:[38,39]

$$\epsilon = \frac{27Dt}{5L^2} \quad (1)$$

Here, D represents the deflection of the substrate, t is the thickness of the PC substrate (250 μm), L is the distance between the two pivotal points (in this work it is fixed as 36 mm). As Figure 1c,d shows, the uniaxial strain was applied from −0.78% (compressive strain) to 0.78% (tensile strain) to study the uniaxial strain's effect on the black phosphorus flake in this work. Afterward, we could apply uniaxial strain along various crystalline orientations of the flake just by manually rotating the sample in accordance with the marks on the edge for every 20° (see Figure 1a–d).

After the target black phosphorus flake is transferred on the PC substrate, the crystalline directions of the flake need to be identified. Herein, we used polarized Raman spectroscopy to identify the specific crystalline orientations of the black phosphorus flake. **Figure 2**a shows the optical image of the black phosphorus flake with a thickness of ≈15 nm (see Figure S2, Supporting Information). We excite the sample (the white dashed boxed area) with a Raman laser of 532 nm wavelength linearly polarized along the horizontal axis and rotate the sample every 20° from 0° to 360° until we obtain the whole full angle-dependent plot of the Raman spectra of the black phosphorus flake. As Figure 2b shows, the spectra contain three characteristic peaks located at 358.5, 437, and 465.5 cm^{-1}, corresponding to the modes A^1_g, B_{2g}, and A^2_g, respectively.[32]

As seen from the spectra, in the first spectrum the Raman peak corresponding to mode A^2_g reaches a maximum and its intensity drops to a minimum when the sample is rotated by 90°. Here we introduce a polar plot to have a better observation of the peak intensity change of three characteristic Raman modes of black phosphorus flake with fitting lines (Figure 2c). For mode A^2_g, one can observe a clear polarized trend on the intensity change of the Raman peak, which reaches a maximum at 0°. Besides, as for mode B_{2g}, a four-loop plot could also be clearly seen. Based on above, one can identify the z-axis (armchair direction) of the black phosphorus flake along the horizontal axis in Figure 2a (along the blue dashed line as Figure 2a shows).

In order to understand the effect of strain on the vibrational properties of black phosphorus, we further carried out the strain-tunable polarized Raman test with our homebuilt four-point bending setup. As **Figure 3**a shows, strain direction, polarized light, and the z-axis of the sample are aligned parallel along the vertical axis initially, then the flake is rotated in a counterclockwise direction, meanwhile, the strain direction and polarized light are fixed during the whole test. Afterward, by rotating the sample from 0° to 360°, we could apply compressive strains from 0% to −0.78% along different crystalline orientations. Figure 3b.1–b.3 shows the Raman spectrum shift of mode A^1_g, B_{2g}, and A^2_g under a compressive strain from 0% to −0.78% when the strain is nearly parallel to z-axis of black phosphorus (167°). A strong and clear blueshift could be observed from mode A^1_g while the peaks shift slightly for mode B_{2g} and mode A^2_g. Interestingly, when one applies the strain nearly-perpendicular to z-axis of black phosphorus flake (75°), as shown in Figure 3b.4–3b.6, mode B_{2g} and mode A^2_g would exhibit a giant blueshift while the mode A^1_g peak barely moves. Note that when the polarized light is fully parallel or perpendicular to the z-axis of black phosphorus, the peak for mode B_{2g} vanishes on the spectra. Afterward, we present a polar plot to better compare the polarized dependence of the Raman shift gauge factor under

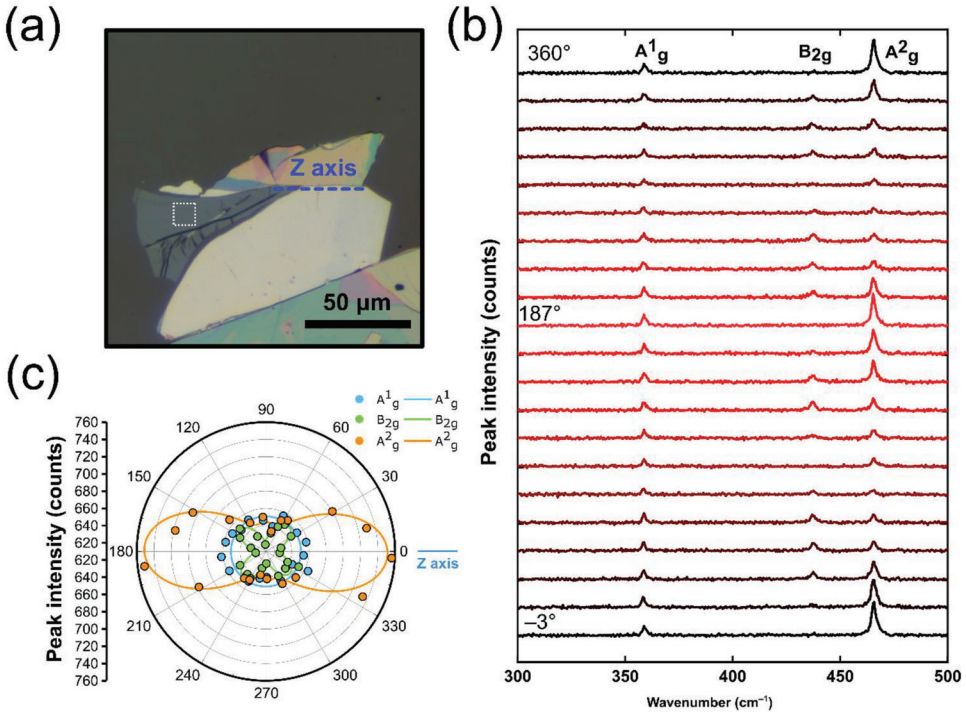

Figure 2. Identification of the crystalline orientation of a BP flake by polarized Raman spectroscopy. a) Optical microscopy image of the BP flake. In the polarization-dependent Raman measurements, the laser is illuminated in the region highlighted with the white dotted square. b) Raman spectra of the BP flake (unstrained) as a function of sample rotation (counterclockwise direction) angle from −3° to 360° (the sample is manually rotated ≈20° and corresponding spectra is recorded after each rotation) while incident light is linearly polarized parallel to the horizontal axis. The spectra have been vertically offset by 120 counts to facilitate the comparison. c) Polar plot of the Raman intensity under A^1_g, B_{2g}, and A^2_g modes for different angles between the polarized light and the cleaved edge of the BP flake, indicating the armchair direction along the horizontal direction and the zigzag direction along the vertical direction.

compressive strain (Figure 3c), which exhibits strong in-plane anisotropic Raman shift for mode A^1_g, B_{2g}, and A^2_g in different ways upon compressive strain. In addition, one can carry out a polarized Raman test of the black phosphorus flake under tensile strain by shifting the positions of the inner cylinders and outer cylinders. In the case of tensile strain, as Figure S3 (Supporting Information) shows, the Raman peaks show a clear redshift under tensile strain from 0% to 0.78% along z-axis for mode A^1_g (7°, Figure S3b.1–b.3, Supporting Information), while for mode B_{2g} and mode A^2_g, the Raman peaks redshift reaches the maximum when strain is applied perpendicular to z-axis (88°, Figure S3b.4–b.6, Supporting Information). Likewise, the polar plot of the Raman shift gauge factor of black phosphorous flake under tensile strain has clearly verified the giant anisotropy of the strain-tunable Raman shift (Figure S3c, Supporting Information).

In order to gain a better and more clear comparison of the peak shift of various Raman modes of black phosphorus under both compressive strain and tensile strain, we present the Raman peak position as a function of strain values under different directions in **Figure 4**. A linear fit is used to extract the gauge factor of the Raman peak shift. One could see that under the same alignment between uniaxial strain and z-axis, the peaks shift similarly in value while in the opposite direction, from which one can deduce that the uniaxial compressive/tensile strain has a similar effect on black phosphorus along a specific crystalline orientation.

In addition, **Table 1** summarizes gauge factors of A^1_g, B_{2g}, and A^2_g Raman modes under tensile/compressive strain applied parallel/perpendicular to z-axis, respectively. It could be seen that the GF of mode A^1_g reaches a maximum of −2.08 (GF_C)/−2.28 (GF_T) cm^{-1}/% when uniaxial strain is applied along z-axis while faints to −0.25 (GF_C)/−0.51 (GF_T) cm^{-1}/% when strain is applied perpendicular to z-axis. Mode B_{2g} shows the strongest response to strain, −4.16 (GF_C)/−5.99 (GF_T) cm^{-1}/% under strain perpendicular to z-axis and −0.51 (GF_C)/−1.41 (GF_T) cm^{-1}/% under strain along z-axis. As for mode A^2_g, the GF shows a maximum of −2.88 (GF_C)/−2.74 (GF_T) cm^{-1}/% when uniaxial strain is applied perpendicular z-axis, which drops to 0.16 (GF_C)/−0.13 (GF_T) cm^{-1}/% when strain is applied along to z-axis. On the basis of the obtained data, the inversed effect of compressive/tensile strain on black phosphorus could be observed. Note that this inversed effect of compressive and tensile strain on the Raman shift of black phosphorus has been studied in the context of theoretical calculation while first been experimentally verified in our study.[40]

In order to have a better understanding on the effect of uniaxial strain on the Raman shift of various vibrational modes in black phosphorus, related DFT calculations of bulk black phosphorus were carried out at the atomic scale. As shown in Figure S4, the layers that make up the BP crystal have a puckered atomic arrangement, unlike 2D materials such as graphene, h-BN, and silicene. This puckered structure emerges thanks to the covalent

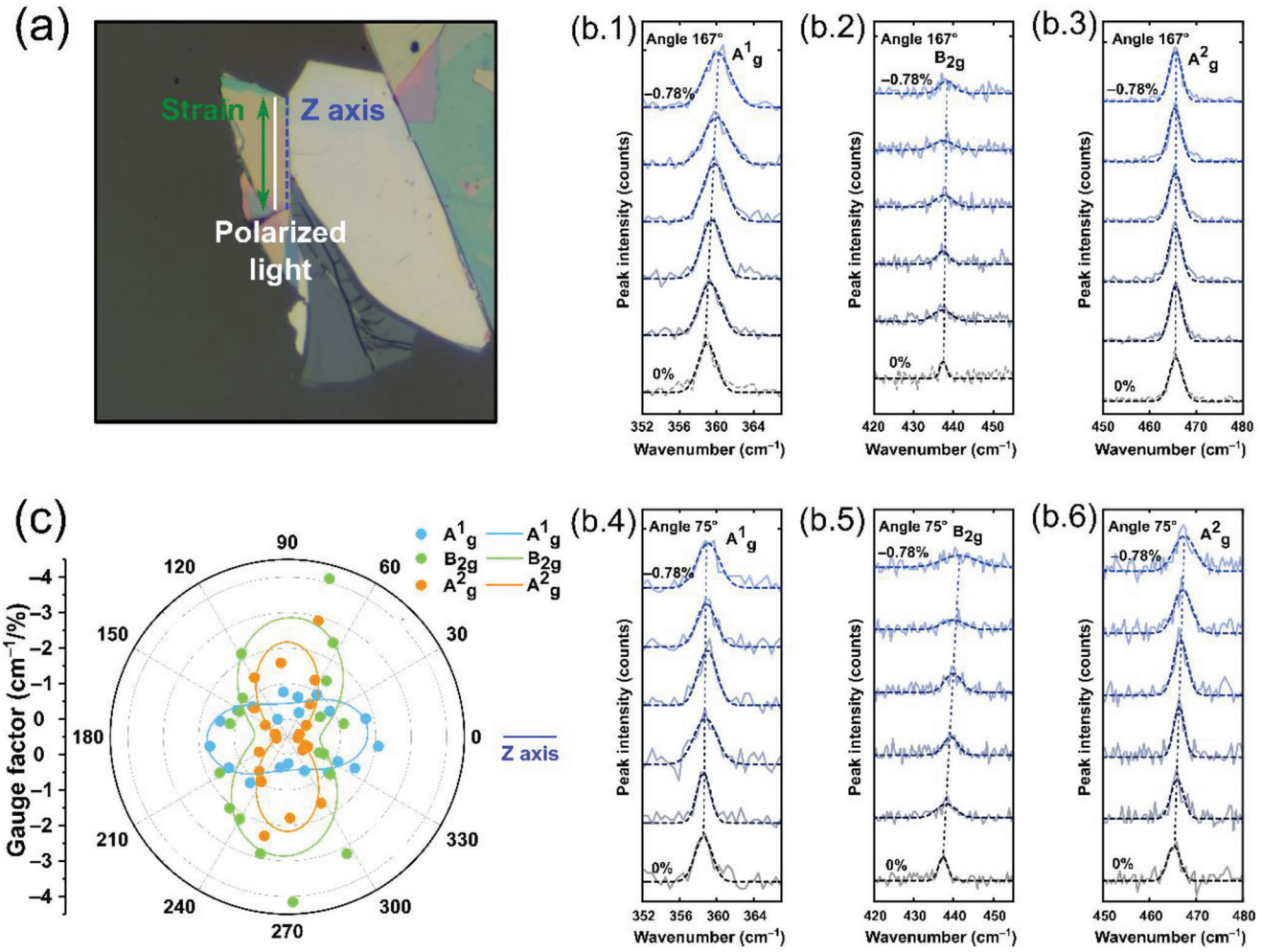

Figure 3. Angle-resolved Raman spectra of BP under different uniaxial compressive strains from 0% to 0.78%. a) Orientation setting in the polarized Raman test under compressive strain. Polarized light, strain direction, and z-axis of the flake are settled parallelly to the vertical axis initially, the flake is rotated in counterclockwise direction while the strain direction and the polarized light are fixed during the whole test. (b1, b2, and b3) Raman spectra comparison under $A^1_g/B_{2g}/A^2_g$ modes collected when the uniaxial compressive strain direction is almost parallel ($\theta = 167°$) to the z-axis of the BP, respectively. (b4, b5, and b6) Raman spectra comparison under $A^1_g/B_{2g}/A^2_g$ modes collected when the uniaxial compressive strain direction is almost perpendicular ($\theta = 75°$) to the z-axis of the BP, respectively. c) Angular dependence of the BP Raman shift gauge factor (peak shift per % of uniaxial compression) as a function of the sample rotation angle in polar coordinates.

bonds between the electrons located in the sp^3 orbitals formed by the hybridized phosphorus atoms with the $3s^2$ $3p^3$ valence electronic configuration. As presented in Figure S4 (Supporting Information), P atoms are connected by bonds of 2.21 Å in the zigzag direction and 2.26 Å in the armchair direction. As a result of this directional bonding between P atoms, the vibrational, electronic, and optical response of the BP crystal has an anisotropic character. In addition, the bonding charge density presented in Figure S5 (Supporting Information) also shows that the hybrid orbitals on the P atoms are concentrated outward from the crystal plane. This indicates that strong interplanar bonding occurs through the electrons in these orbitals. Therefore, it can be expected that the response of the crystal structure to external strain will have both in-plane and out-of-plane characteristics, regardless of the direction of application of the strain.

Based on above, we further investigated the strain dependency of θ_1 and θ_2 bond angles in Figure S4 (Supporting Information). As presented in Figures S6 and S7 (Supporting Information), apparently, while θ_1 has a strong dependence on strains applied along the ZZ direction, θ_2 is more responsive against strains against AC directions. In addition, ZZ strain-induced modifications in θ_1 also result in slight changes in AC. This shows us that compressive or tensile strain applied in the ZZ direction also affects the crystal structure in the AC direction (with a reverse effect). As a result, strain effect can be expected to be seen as opposite to each other in phonons that have vibration in ZZ and AC directions.

The nature of the interlayer interaction in the BP crystal is much more complex than in materials such as graphene. The out-of-plane interaction in graphene, which occurs simply through electrons in the p_z orbitals, has a more complex nature because of the tilted hybrid orbitals in the BP crystal. Therefore, there are two more structural parameters that need to be defined to understand the interlayer interaction, these are d_{ZZ} and d_{AC}.

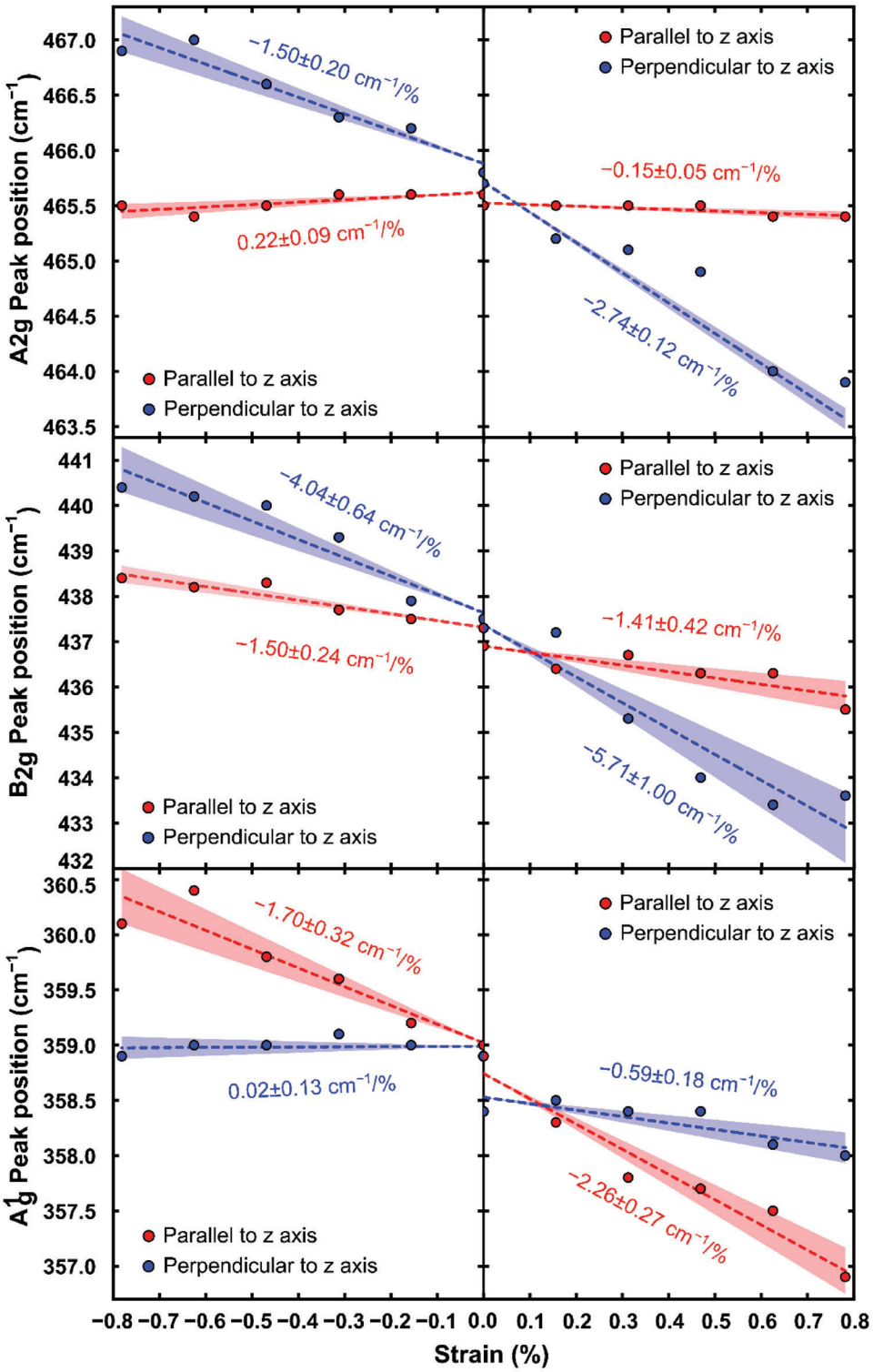

Figure 4. Raman shift at $A^1_g/B_{2g}/A^2_g$ modes as a function of the applied uniaxial compressive and tensile strain from 0% to −0.78%/0.78% applied parallel and perpendicular to z-axis, respectively. A linear fit is used to extract the gauge factor. The shaded area around the dashed lines represents the uncertainty of the gauge factor extracted from the linear fit.

Table 1. Summary of gauge factor comparison of A^1_g, B_{2g}, and A^2_g Raman modes under tensile/compressive strain applied parallel/perpendicular to z-axis.

BP sample		GF_C [cm^{-1}/%, compression, 0% to −0.78%]		GF_T [cm^{-1}/%, tension, 0% to 0.78%]	
		Parallel to z-axis	Perpendicular to z-axis	Parallel to z-axis	Perpendicular to z-axis
Raman Mode	A^1_g	−2.08	−0.25	−2.28	−0.51
	B_{2g}	−0.51	−4.16	−1.41	−5.99
	A^2_g	0.16	−2.88	−0.13	−2.74

As shown in Figure S8 (Supporting Information), a P atom in a layer has two closest neighbors in the out-of-plane direction. They are in the ZZ and AC directions. d_{ZZ} is shorter and the interlayer interaction in this direction is stronger than the interaction in the AC direction. Our calculations presented in Figure S9 (Supporting Information) also reveal that in-plane strain is able to tune out-of-plane interaction as well. In addition, AC direction strain exhibits a higher tunability on the d_{ZZ} and d_{AC} compared with ZZ direction strain, meanwhile, ZZ direction strain exhibits slight tunability on the d_{AC}.

On the basis of these findings, one can get insight into the anisotropic strain-tunable Raman shift behind. In order to better understand the observed trends one can use a simplified mechanical model based on 6 structural parameters: R_1, R_2, d_{ZZ}, and d_{AC} that represent the P—P distances and θ_1 and θ_2 that are two bond angles (Figure S10, Supporting Information).[32] Basically, the A^2_g mode of black phosphorus is orthogonal to the A^1_g mode and B_{2g} mode is totally along the in-plane direction. When the compressive strain is applied along the ZZ-axis (perpendicular to z-axis), R_1 is compressed and θ_1 is shrunken. This modification of R_1 and θ_1 leads to a giant blueshift of B_{2g} and A^2_g modes while A^1_g is not affected because the vibration of A^1_g is along the out-of-plane direction. On the other hand, when the compressive strain is applied along AC axis (z-axis), θ_2 and d_{ZZ} are reduced a lot and R_1 is compressed slightly as well. Normally, one doesn't expect such a strong dependence between in-plane strain and out-of-plane phonon mode but, as shown in Figure S9 (Supporting Information), d_{ZZ} and d_{AC} have a linearly increasing trend with increasing in-plane strain. Therefore, the in-plane strain-induced blueshift in A^1_g phonon mode can be expected. Apart from this, according to Li's work, reduced θ_2 generates a shear-like motion between two nearby sublayers.[32] The out-of-plane restoring force between two sublayers is strengthened while the in-plane force is weakened, leading to the enhancement of A^1_g mode and the softening of A^2_g mode. Meanwhile, the slightly compressed R_1 enhances A^2_g and B_{2g} modes. Thus, a blueshift of A^1_g and B_{2g} could be observed, while A^2_g does not shift much as a result of neutralization. As for tensile strain, reversed regulations on the bond lengths and bond angles could lead to a redshift on the frequency of optical modes while shows a similar trend numerically. Note that our experimental data obtained under tensile strain are in good agreement with experimental study by Lau and theoretical study reported by Karki,[32,40] which shows pretty similar Raman shift trend of mode A^1_g, B_{2g}, and A^2_g under tensile strain compared with our study. Nevertheless, in Karki's work, mode A^1_g shows a giant shift under strain along ZZ direction, while it barely shifts in our study. This phenomenon might result from the thickness difference that leads to a difference on the P—P d_{ZZ} and d_{AC}, further affect the interaction between layers.

Further the reproducibility test was carried out by applying 5 compressive strain cycles on the black phosphorus flake parallel and perpendicular to z-axis, respectively. Figures S11 and S12 (Supporting Information) show the Raman shift of mode A^1_g and A^2_g as a function of the applied uniaxial compressive strain from 0% to −0.78%, from which one could observe a perfect reproducibility after 5 strain applying/releasing cycles. Also, Raman spectra of mode A^1_g and mode A^2_g acquired under a compressive strain cycle from 0% to −0.78% to 0% also present an excellent reproducibility (see Figure S13, Supporting Information), which is also a strong proof of the outstanding strain applicability of the homebuilt four-point bending setup.

3. Conclusion

In summary, we developed a four-point bending apparatus that could offer a route to apply both compressive strain and tensile strain along different crystal directions to in-plane anisotropic 2D materials. Polarized Raman spectroscopy was utilized to study the effect of uniaxial compressive/tensile strain on the vibrational property of black phosphorus. The Raman peaks corresponding to mode A^1_g, mode B_{2g}, and mode A^2_g presented a strong anisotropic blueshift/redshift under compressive/tensile strain along different directions. Particularly, when the strain was applied parallel/perpendicular to the z-axis of black phosphorus, Raman shift of mode A^1_g exhibited a maximum/minimum while mode B_{2g} and mode A^2_g reached a minimum/maximum, which is due to the strain's effect on the regulation of the bond angle and length, and interlayer interaction based on DFT calculations. Our work paves a way to explore the anisotropic strain-resolved electrical, optical, and optoelectrical properties of related 2D anisotropic materials-based stretchable devices.

4. Experimental Section

Exfoliation of Black Phosphorus Flakes: Commercial bulk black phosphorus was bought from HQ Graphene company. Nitto tape (Nitto SPV 224) was adhered to the commercial bulk black phosphorus to peel off the bulk crystals, then relatively-thinner bulk crystals were obtainted by adhering another Nitto tape on the top of the first Nitto tape sample and repeating this process for several times. In order to obtain the final few-layered black phosphorus flakes a piece of Gel-Film (Gel-Pak, WF ×4 6.0 mil) was adhered on the Nitto tape sample and peeled off gently. Further accurate identification of the thickness of black phosphorus flakes could be carried out by Atomic Force Microscopy after transfer.

Transfer of Black Phosphorus Flakes on Disk-Like Polycarbonate Substrate: Once the target black phosphorus flake was found, it was transferred on the center of the disk-like polycarbonate substrate (Modulor) with a thickness of 250 µm by an all-dry deterministic placement method.[35]

Identification of Crystalline Orientation of Black Phosphorus Sample: A linearly polarized Raman laser of 532 nm was used to excite the samples. A 50X objective lens was used to focus the laser onto the sample with a spot size of ≈1.0 µm. Also, the power of incident laser on the sample was decreased to 0.103 mW to prevent the degradation of the exfoliated BP under heating. First, the analyzer and polarizer of the Raman system were adjusted to make sure they were aligned parallel to the horizontal axis. Second, the substratewith black phosphorus was settled under the objective (50X) lens, with red marker on the edge parallel to the horizontal axis. Third, the Raman spectrum of the flake was collected under rotating angle from 0° to 360° by 20°. Finally, by analyzing the intensity change of various Raman modes the crystalline direction of the flake (zigzag and armchair directions) were identified.

Strain-Resolved Raman Spectroscopy: Once the sample was placed on the four-points bending apparatus, the setup was mounted under the objective (50X) of the optical microscope that was integrated with a polarized Raman system for collecting the spectra. The flake was settled in the center of two inner pivots under microscope, note that for four-point bending setup, each point on the area between the inner pivots should sustain equal strain. The z-axis of the flake , strain direction, and the polarized light direction was set, parallel to the vertical axis, as the initial position. Further, the Raman spectrums were acquired under different uniaxial strain levels from 0% to 0.78% (strain step of 0.156%), which was released to 0% after the test. Afterward, the sample was rotated by 20° according to the markers on the substrate edge and the spectrums were collected likewise. Eventually, one could collect the polarized Raman spectrums by rotating the sample from 0° to 360° to apply the strain along different crystalline directions.

Further angular dependence of Raman shift rate was fitted with the formula below:

$$y = y_0 + \left(\left(a * \sin(pi * x/180 + d)^2\right) + c * \cos(pi) * \cos(pi * x/180 + d)^2\right)^2 + c^2 * \sin(pi)^2 * \cos(pi * x/180 + d)^4 \quad (2)$$

Computational Methodology: Theoretical calculations for pristine and strained BP crystals were carried out in the framework of density functional theory (DFT).[41] The generalized gradient approximation (GGA) of Perdew–Burke–Ernzerhof (PBE) was used for the exchange-correlation function.[42] DFT-D2 method was used for the van der Waals (vdW) correction.[43] The kinetic energy cutoff for plane-wave expansion was set to 500 eV and the energy was minimized until its variation became 10^{-8} eV. For structural relaxation calculations, cut-off of total Hellmann–Feynman forces was set to to 10^{-7} eV A^{-1}. $8 \times 8 \times 1$ Γ centered k-point samplings were used for structural relaxation in primitive cell. To calculate the Raman activity of phonon modes under uniaxial strain, a rectangular unit cell with one side parallel to the direction of stretch was considered.

Supporting Information

Supporting Information is available from the Wiley Online Library or from the author.

Acknowledgements

This work was funded by the European Research Council (ERC) under the European Union's Horizon 2020 research and innovation program (grant agreement no 755655, ERC-StG 2017 project 2D-TOPSENSE), the Ministry of Science and Innovation (Spain) through the project PID2020-115566RB-I00. The authors also acknowledge funding from the EU FLAG-ERA project To2Dox under the program PCI2019-111893-2. H.L. acknowledges the grant from the China Scholarship Council (CSC) under no. 201907040070.

Conflict of Interest

The authors declare no conflict of interest.

Data Availability Statement

The data that support the findings of this study are available from the corresponding author upon reasonable request.

Keywords

black phosphorus, deterministic transfer, Raman spectroscopy, uniaxial strain

Received: June 23, 2023
Revised: August 24, 2023
Published online:

[1] G. G. Naumis, S. Barraza-Lopez, M. Oliva-Leyva, H. Terrones, *Rep Prog Phys* **2017**, *80*, 096501.
[2] R. Roldán, A. Castellanos-Gomez, E. Cappelluti, F. Guinea, *J. Phys.: Condens. Matter* **2015**, *27*, 313201.
[3] F. Guinea, M. I. Katsnelson, A. K. Geim, *Nat. Phys.* **2010**, *6*, 30.
[4] S. Deng, A. V. Sumant, V. Berry, *Nano Today* **2018**, *22*, 14.
[5] W. Liu, M. Liu, R. Ma, R. Zhang, W. Zhang, D. Yu, Q. Wang, J. Wang, H. Wang, *Adv. Funct. Mater.* **2018**, *28*, 1705928.
[6] W. Tian, L. Min, F. Cao, L. Li, *Adv. Mater.* **2020**, *32*, 1906974.
[7] W. Gao, S. Emaminejad, H. Y. Y. Nyein, S. Challa, K. Chen, A. Peck, H. M. Fahad, H. Ota, H. Shiraki, D. Kiriya, D.-H. Lien, G. A. Brooks, R. W. Davis, A. Javey, *Nature* **2016**, *529*, 509.
[8] A. Chortos, J. Liu, Z. Bao, *Nat. Mater.* **2016**, *15*, 937.
[9] J. Lee, T.-H. Han, M.-H. Park, D. Y. Jung, J. Seo, H.-K. Seo, H. Cho, E. Kim, J. Chung, S.-Y. Choi, T.-S. Kim, T.-W. Lee, S. Yoo, *Nat. Commun.* **2016**, *7*, 11791.
[10] T. Yu, Y. Hu, G. Feng, K. Hu, *Adv. Ther.* **2020**, *3*, 1900195.
[11] T. Ahmed, S. Kuriakose, E. L. H. Mayes, R. Ramanathan, V. Bansal, M. Bhaskaran, S. Sriram, S. Walia, *Small* **2019**, *15*, 1900966.
[12] S. Bertolazzi, J. Brivio, A. Kis, *ACS Nano* **2011**, *5*, 9703.
[13] W. Li, X. Qian, J. Li, *Nat. Rev. Mater.* **2021**, *6*, 829.
[14] K.-A. N. Duerloo, Y. Li, E. J. Reed, *Nat. Commun.* **2014**, *5*, 4214.
[15] P. Gant, P. Huang, D. Pérez de Lara, D. Guo, R. Frisenda, A. Castellanos-Gomez, *Mater. Today* **2019**, *27*, 8.
[16] K. He, C. Poole, K. F. Mak, J. Shan, *Nano Lett.* **2013**, *13*, 2931.
[17] A. Castellanos-Gomez, R. Roldán, E. Cappelluti, M. Buscema, F. Guinea, H. S. J. van der Zant, G. A. Steele, *Nano Lett.* **2013**, *13*, 5361.
[18] E. Khestanova, F. Guinea, L. Fumagalli, A. K. Geim, I. V. Grigorieva, *Nat. Commun.* **2016**, *7*, 12587.
[19] H. Li, A. W. Contryman, X. Qian, S. M. Ardakani, Y. Gong, X. Wang, J. M. Weisse, C. H. Lee, J. Zhao, P. M. Ajayan, J. Li, H. C. Manoharan, X. Zheng, *Nat. Commun.* **2015**, *6*, 7381.
[20] G. H. Ahn, M. Amani, H. Rasool, D.-H. Lien, J. P. Mastandrea, J. W. Ager Iii, M. Dubey, D. C. Chrzan, A. M. Minor, A. Javey, *Nat. Commun.* **2017**, *8*, 608.
[21] T. M. G. Mohiuddin, A. Lombardo, R. R. Nair, A. Bonetti, G. Savini, R. Jalil, N. Bonini, D. M. Basko, C. Galiotis, N. Marzari, K. S. Novoselov, A. K. Geim, A. C. Ferrari, *Phys. Rev. B* **2009**, *79*, 205433.

[22] F. Carrascoso, R. Frisenda, A. Castellanos-Gomez, *Nano Materials Science* **2022**, *4*, 44.
[23] I. Niehues, R. Schmidt, M. Drüppel, P. Marauhn, D. Christiansen, M. Selig, G. Berghäuser, D. Wigger, R. Schneider, L. Braasch, R. Koch, A. Castellanos-Gomez, T. Kuhn, A. Knorr, E. Malic, M. Rohlfing, S. Michaelis de Vasconcellos, R. Bratschitsch, *Nano Lett.* **2018**, *18*, 1751.
[24] I. Niehues, A. Blob, T. Stiehm, S. Michaelis de Vasconcellos, R. Bratschitsch, *Nanoscale* **2019**, *11*, 12788.
[25] Z. Li, Y. Lv, L. Ren, J. Li, L. Kong, Y. Zeng, Q. Tao, R. Wu, H. Ma, B. Zhao, D. Wang, W. Dang, K. Chen, L. Liao, X. Duan, X. Duan, Y. Liu, *Nat. Commun.* **2020**, *11*, 1151.
[26] X. He, H. Li, Z. Zhu, Z. Dai, Y. Yang, P. Yang, Q. Zhang, P. Li, U. Schwingenschlogl, X. Zhang, *Appl. Phys. Lett.* **2016**, *109*, 173105.
[27] A. P. John, A. Thenapparambil, M. Thalakulam, *Nanotechnology* **2020**, *31*, 275703.
[28] F. Carrascoso, H. Li, R. Frisenda, A. Castellanos-Gomez, *Nano Res.* **2021**, *14*, 1698.
[29] D. Xu, J. Tan, H. Hu, G. Ouyang, *Phys. Chem. Chem. Phys.* **2022**, *24*, 22806.
[30] L. Zhang, H. Li, C. Sun, G. Ouyang, *J. Raman Spectrosc.* **2020**, *51*, 213.
[31] Y. Wang, S. Yao, P. Liao, S. Jin, Q. Wang, M. J. Kim, G. J. Cheng, W. Wu, *Adv. Mater.* **2020**, *32*, 2002342.
[32] Y. Li, Z. Hu, S. Lin, S. K. Lai, W. Ji, S. P. Lau, *Adv. Funct. Mater.* **2017**, *27*, 1600986.
[33] W. Zhu, L. Liang, R. H. Roberts, J.-F. Lin, D. Akinwande, *ACS Nano* **2018**, *12*, 12512.
[34] W. Luo, A. D. Oyedele, Y. Gu, T. Li, X. Wang, A. V. Haglund, D. Mandrus, A. A. Puretzky, K. Xiao, L. Liang, X. Ling, *Adv. Funct. Mater.* **2020**, *30*, 2003215.
[35] H. Li, G. Sanchez-Santolino, S. Puebla, R. Frisenda, A. M. Al-Enizi, A. Nafady, R. D'Agosta, A. Castellanos-Gomez, *Adv. Mater.* **2022**, *34*, 2103571.
[36] H. Li, D.-Y. Lin, A. Di Renzo, S. Puebla, R. Frisenda, X. Gan, J. Quereda, Y. Xie, A. M. Al-Enizi, A. Nafady, A. Castellanos-Gomez, *Appl. Phys. Lett.* **2022**, *120*, 063101.
[37] R. Frisenda, E. Navarro-Moratalla, P. Gant, D. Pérez De Lara, P. Jarillo-Herrero, R. V. Gorbachev, A. Castellanos-Gomez, *Chem. Soc. Rev.* **2018**, *47*, 53.
[38] Y. N. Loginov, S. I. Stepanov, A. I. Golodnov, G. Z. Mukanov, *KnE Engineering* **2019**, *4*, 106.
[39] P. Costa, A. Ferreira, V. Sencadas, J. C. Viana, S. Lanceros-Méndez, *Sens. Actuator A Phys.* **2013**, *201*, 458.
[40] B. Karki, B. Freelon, M. Rajapakse, R. Musa, S. M. S. Riyadh, B. Morris, U. Abu, M. Yu, G. Sumanasekera, J. B. Jasinski, *Nanotechnology* **2020**, *31*, 425707.
[41] P. E. Blöchl, *Phys. Rev. B* **1994**, *50*, 17953.
[42] J. P. Perdew, K. Burke, M. Ernzerhof, *Phys. Rev. Lett.* **1996**, *77*, 3865.
[43] S. Grimme, *J. Comput. Chem.* **2006**, *27*, 1787.